



# Realisation of Fractal Grid-Induced Turbulence Strength with PTFV: Effects of Grid Geometry

Ted Sian Lee<sup>1</sup> · Ean Hin Ooi<sup>1</sup> · Wei Sea Chang<sup>1</sup> · Ji Jinn Foo<sup>1</sup>

Received: 9 May 2023 / Accepted: 22 August 2023 / Published online: 16 September 2023  
© The Author(s) 2023

## Abstract

The unravelling of multilength-scale insert-generated turbulence, particularly, the induced-forcing plays critical role in the fundamental comprehension of energy formation and decay as a function of grid conformation. This study experimentally investigates the flow mechanical characteristics at  $Re_{Dh} = 4.1 \times 10^4$  for a regular-grid (RG), single-square-grid (SSG) and six 2D planar space-filling square-fractal-grids (SFG) of different fractal iterations ( $N$ ), thickness ratios ( $t_r$ ) and blockage ratios ( $\sigma$ ) via piezoelectric thin-film flapping velocimetry (PTFV). Thin-film's tip-deflection ( $\delta_{rms}$ ) and voltage response ( $V_{rms}$ ) analysis along the grids' centreline reveals increasing flow fluctuation strength with increasing  $\sigma$ ,  $t_r$  and decreasing  $N$ , owing to higher shedding intensity of lower frequency, larger scale energy-containing vortices from thicker first iteration bar. However, higher: energy dissipation rate, centreline mean velocity decrement rate and local deceleration experienced in the turbulence decay region of larger  $t_r$  grid, along with additional fractal scales lead to less potent flow-structure-interplay on thin-film undulation. More importantly, SSG-generated turbulence enables the generation of average ( $V_{rms}$ ,  $\delta_{rms}$ ) and millinewton turbulence forcing  $F_{rms}$  that are respectively, 9× and 5× larger than RG of similar  $\sigma$ , and 2× larger than the best performing  $N=3$  SFG. Our findings disclose the importance of grid geometrical management for effective utilisation of turbulence-generating grids in engineering applications.

**Keywords** Fluid–structure interaction · Piezoelectric thin-film flapping · Fractal · Grid-induced turbulence · Flow fluctuation · Turbulence forcing

## 1 Introduction

Corrugated surfaces (Tinney et al. 2020; Guilarte Herrero et al. 2021), flaps (Li et al. 2002; Rosti et al. 2018) and turbulence-generating grids (Batchelor and Townsend 1947; Comte-Bellot and Corrsin 1966; Geipel et al. 2010; Fragner et al. 2015) are examples of passive

---

✉ Ted Sian Lee  
ted.lee@monash.edu

✉ Ji Jinn Foo  
foo.ji.jinn@monash.edu

<sup>1</sup> Mechanical Engineering Discipline, School of Engineering, Monash University Malaysia, 47500 Sunway City, Selangor, Malaysia

flow control techniques widely adopted to generate fluid flow perturbations to alter the flow field to a desired state. The turbulence generated by planar fractal grids, which comprise self-repeating patterns superimposed at multiple scales, have been extensively studied both experimentally (Hurst and Vassilicos 2007; Valente and Vassilicos 2011; Nagata et al. 2013; Goh et al. 2021) and numerically (Laizet and Vassilicos 2011; Suzuki et al. 2013; Zhou et al. 2014; Mok et al. 2023) over the past decade and a half. Pioneering work by Hurst and Vassilicos (2007) has discovered the existence of a protracted turbulence generation region in the lee of square fractal grid (SFG), where the centreline turbulence intensity increases progressively to a peak, followed by a decay region. It is acknowledged that regular grid (RG) generates higher centreline turbulence intensity peak over a short region very close to the grid than SFG of the same blockage ratio  $\sigma$  and effective mesh size  $M_{eff}^1$  (Laizet and Vassilicos 2011; Melina et al. 2016). Nevertheless, the higher vorticity and turbulence intensity flow produced by SFG in the protracted region (Laizet and Vassilicos 2011) makes SFG highly attractive for thermal mixing (Teh et al. 2015; Skanathan et al. 2018), convective heat transfer (Hoi et al. 2019a, b) and energy harvesting (Ferko et al. 2019a, b) applications.

In general, grid turbulence can be divided into the near-field and far-field regions (Simmons and Salter 1934; Hearst and Lavoie 2016). The non-equilibrium near-field is identified as the region that experiences strong cross-stream inhomogeneities in which its turbulence evolution is directly influenced by the initial flow generating conditions (Hearst and Lavoie 2016). As one goes sufficiently far downstream, the homogeneous far-field turbulence generated by SFG behaves as one might expect for an RG undergoing power-law decay (Hearst and Lavoie 2014, 2016). While rapid decay also exists close to the RG (Krogstad and Davidson 2012; Isaza et al. 2014), when the mesh length of RG is made identical to the largest grid bar length  $L_0$  of SFG with both grids having equivalent  $\sigma$ , the extended region of rapid decay in the lee of SFG relative to RG results in a less energetic far-field (Hearst and Lavoie 2016). Therefore, apart from producing stronger turbulent diffusion and higher scalar mixing (Nedić and Tavoularis 2016), RG also generates higher turbulence intensity and Taylor microscale Reynolds number  $Re_\lambda$  than the SFG in the far-field region (Hearst and Lavoie 2016). This contradicts the assertion that the scalar diffusion behind SFG is more efficient than RG, since the mesh sizes of the RGs used by Suzuki et al. (2010) and Laizet and Vassilicos (2015) were much smaller than the  $L_0$  of SFG.

Hitherto, various research has been undertaken to examine the interesting interplay between the SFG geometric parameters and the unique multilength-scale flow generated. While the magnitude of the turbulence intensity peak is reported to be proportional to the ratio of the width to the length of largest grid bar  $t_0/L_0$  (Gomes-Fernandes et al. 2012), its peak distance  $x_{peak}$  can be approximated from the wake-interaction length scale (Mazellier and Vassilicos 2010; Gomes-Fernandes et al. 2012), which represents the location on the centreline where the wakes from the largest grid bars encounter each other. It was discovered that an increase in thickness ratio  $t_r$ , (the ratio of largest to smallest bar width) shortens the  $x_{peak}$  but at the same time increases the turbulence intensity and Reynolds number of the generated flow (Hurst and Vassilicos 2007; Mazellier and Vassilicos 2010). Weitemeyer et al. (2013) experimentally showed that the turbulence intensity heightens with increasing  $\sigma$ , whilst  $x_{peak}$  is pushed further downstream with the addition of a fourth iteration to

<sup>1</sup>  $M_{eff} = \frac{4T^2}{P} \sqrt{1 - \sigma}$  (Hurst and Vassilicos 2007), where  $T^2$  is the tunnel's square cross section and  $P$  the grid perimeter length.

the SFG design. This is further supported by the experiments conducted by Omilion et al. (2018) where the high turbulence intensity leeward of SFG displays an elongated trend when additional fractal scales are added to the grid. Moreover, Nagata et al. (2017) demonstrated that the smallest grid elements of higher iteration SFG plays a significant role for the nearly constant Taylor microscale and integral length scale detected in the turbulence decay region. On the other hand, the presence of smaller geometrical iterations in SFG with fractal iteration  $N=4$  could lead to a less intense vortex shedding effects along the centreline as compared to a single square grid (SSG) (Melina et al. 2016).

All the above-mentioned experimental studies employ either costly hot wire anemometry (HWA) or particle image velocimetry (PIV) to quantitatively detect turbulence. The qualitative characterisation of fractal grid-induced turbulence based upon the direct interaction of the flow with a piezoelectric thin-film has only been recently initiated (Ferko et al. 2018; Ferko et al. 2019a, b; Lee et al. 2021). In the previous experimental work by Lee et al. (2021), mechanical characteristic of the centreline streamwise and cross-sectional turbulence generated from a space-filling SFG and RG with comparable  $\sigma$  and  $M_{eff}$  were experimentally unveiled via piezoelectric thin-film flapping velocimetry (PTFV). Analysis of the thin-film's physical response revealed the superior advantages of SFG-generated turbulence over RG in terms of flow fluctuation strength and the corresponding turbulence forcing (turbulence-induced excitation force acting on the thin-film).

In view of the significant impact of grid geometry on the flow generated by an SFG and RG, a parametric study on the effects of SFG design towards the resulting turbulence mechanical characteristics is of utmost importance for effective utilisation of fractal grids in a wide variety of engineering applications. To date, the interplay between the grid geometric parameters and the mechanical characteristics of SFG-generated flow, particularly the turbulence forcing has yet to be explored. There also appears to be limited work on the individual influence of different  $\sigma$  and  $N$  towards the resulting flow characteristics, as the  $\sigma$  is not held constant in most studies (Nagata et al. 2017; Omilion et al. 2018) involving SFG of different fractal scales. Furthermore, the SFGs tested in the majority of the research (Hurst and Vassilicos 2007; Laizet and Vassilicos 2011; Valente and Vassilicos 2011; Nagata et al. 2013; Hearst and Lavoie 2016; Goh et al. 2021) are of low to medium  $\sigma$  with  $\sigma < 0.4$ . Essentially, the turbulent wakes and jets generated by high  $\sigma$  grid would become unstable, and the resulting turbulence is less likely to be homogeneous besides taking longer to reach uniformity (Corrsin 1963). However, through careful fine-tuning of the fractal-fin geometrical parameters, the intense turbulence level and vigorous flow fluctuation characteristics of the flow generated by SFG, partially-covered SFG and partially-covered RG with  $\sigma=0.49$  have been recently proven to be highly critical and preferable in enhancing the thermal dissipation of plate-fin heat sink (Hoi et al. 2019a, 2022; Chew et al. 2022). In addition, the potent flow fluctuation strength and turbulence forcing induced by SFG of  $\sigma=0.49$  allows high piezoelectric voltage output to be secured, thus presenting promising prospect for fluidic energy harvesting from high-blockage SFG-induced turbulence (Lee et al. 2021).

Hence, the present work seeks to investigate the fluid–structure interaction between a flexible piezoelectric thin-film and the flow generated by different geometric parameters high-blockage passive grids via in-house PTFV (Lee et al. 2021). Since the piezoelectric thin-film immersed in insert-generated flow domain flaps to generate voltage as a function of fluid flow undulation, the tip deflection and voltage response of a polyvinylidene fluoride (PVDF) piezoelectric cantilever beam are measured at various centreline streamwise distances leeward of an RG, an SSG and six SFGs of different  $N$ ,  $t_r$ , and  $\sigma$  to disclose the respective flow fluctuation strength. The local equivalent turbulence statistics determined

from the film undulation are also analysed to provide insights into the insert-induced centreline streamwise turbulent flow characteristics and induced forcing. The in-house developed PTFV would serve as a potential candidate for a low cost, in situ qualitative evaluation of the fundamental mechanical characteristics of the turbulent flow structures generated by SFGs of different geometric parameters, such that the SFG-generated flow can be better manipulated by restructuring the flow through proper turbulence management to best match the intended application. At the same time, the voltage data acquired from experiments could be particularly useful for future energy harvesting studies. For instance, piezoelectric thin-film could be placed in the lee of the turbulator that induces greatest piezoelectric voltage generation to maximise the electrical energy harvested for self-powering low-power sensors to monitor, control, and manage heating, ventilation and air conditioning (HVAC) systems.

## 2 Methods

### 2.1 Turbulence-Generating Grids

A total of eight turbulence-generating grids [Grid<sub>N</sub><sup>t</sup>( $\sigma$ )] made from 10 mm thick transparent acrylic sheet are examined in this study: a regular grid [RG(0.492)], a single square grid [SSG(0.493)] and six different 2D planar space-filling square fractal grids [SFG<sub>2</sub><sup>6.5</sup>(0.493), SFG<sub>3</sub><sup>6.5</sup>(0.493), SFG<sub>3</sub><sup>6.5</sup>(0.382), SFG<sub>3</sub><sup>6.5</sup>(0.270), SFG<sub>3</sub><sup>4.0</sup>(0.493), SFG<sub>3</sub><sup>9.8</sup>(0.493)]. The schematic of the grids along with their geometrical details are presented in Fig. 1 and Table 1, respectively. Note that  $A_o$  denotes the grid's central opening area and  $x_*$  the wake-interaction length scale.  $x_*$  was first introduced by Mazellier and Vassilicos (2010) as,

$$x_* = \frac{L_0^2}{t_0} \quad (1)$$

where  $L_0$  and  $t_0$  are the length and lateral thickness (width) of the largest grid bar, respectively. Equation 1 has been widely used in literature (Laizet and Vassilicos 2011; Laizet et al. 2015; Hearst and Lavoie 2016; Melina et al. 2016; Nedić and Tavoularis 2016; Nagata et al. 2017) to compute  $x_*$  with the intention of providing an estimation of the centreline turbulence intensity peak location and also to normalise the results obtained for fractal grids of different geometric characteristics. By taking into consideration the effect of inlet free-stream turbulence on the wake development in a water tunnel, Gomes-Fernandes et al. (2012) proposed a new wake-interaction length scale  $x_*^{peak}$ ,

$$x_*^{peak} = 0.21 \frac{L_0^2}{\alpha C_d t_0} \quad (2)$$

where  $C_d$  is the drag coefficient, while  $\alpha$  refers to the parameter that takes into account the free-stream turbulence intensity and length scale. Considering that the free-stream turbulence is negligible for wind tunnel experiments (Gomes-Fernandes et al. 2012),  $x_*$  is calculated using Eq. 1 for the present study.

The RG considered here (Fig. 1h) has a blockage ratio (ratio of lateral plane area covered by grid to tunnel cross-sectional area)  $\sigma = 0.492$ , and its geometry is the same as that used by Lee et al. (2021). Apart from SSG (Fig. 1a) and SFG<sub>2</sub> (Fig. 1b) where both inserts are supported at the corners by four struts with 3 mm lateral thickness, the

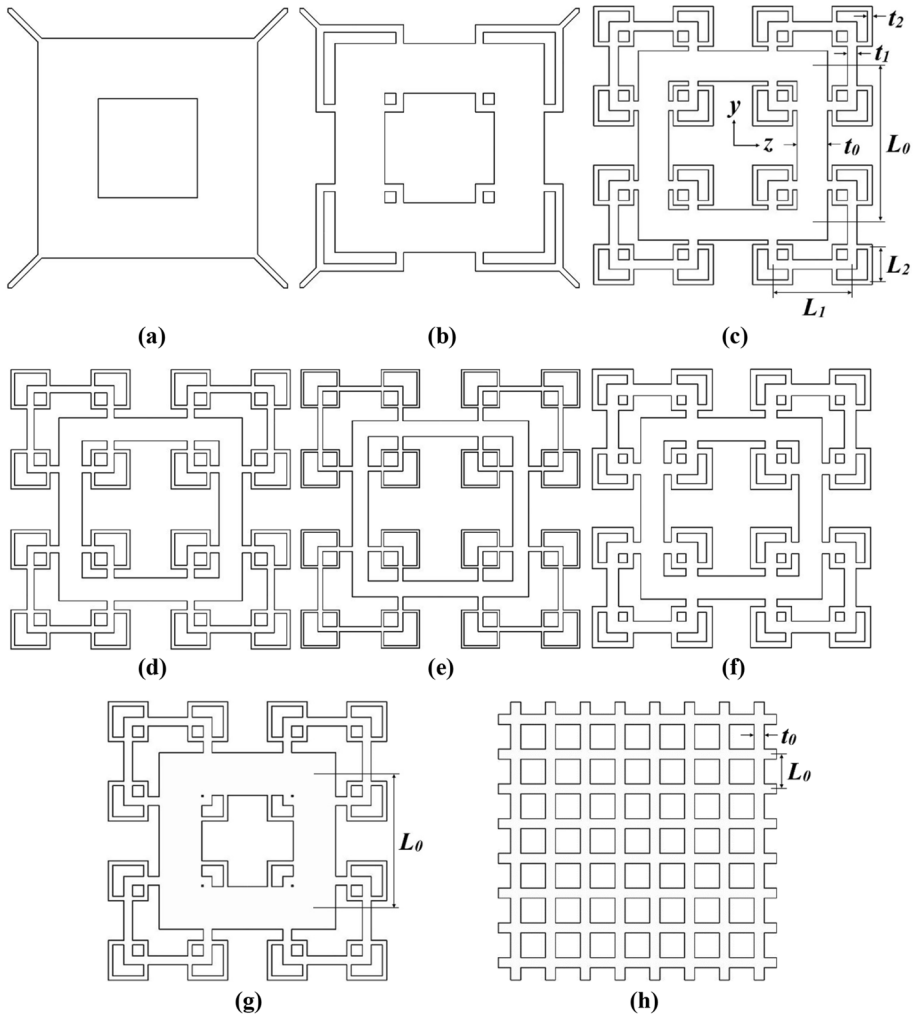


**Fig. 1** Schematic of the turbulence-generating grids: **a** SSG(0.493), **b** SFG<sub>2</sub><sup>6.5</sup>(0.493), **c** SFG<sub>3</sub><sup>6.5</sup>(0.493), **d** SFG<sub>3</sub><sup>6.5</sup>(0.382), **e** SFG<sub>3</sub><sup>6.5</sup>(0.270), **f** SFG<sub>3</sub><sup>4.0</sup>(0.493), **g** SFG<sub>3</sub><sup>9.8</sup>(0.493) (Hoi et al. 2019a), and **h** RG(0.492) (Lee et al. 2021) [note Grid<sub>N</sub><sup>t<sub>r</sub></sup>(σ)]

rest of the inserts have cross-sectional area equivalent to the test section. All SFGs and SSG are designed to have almost similar first, second and third iterative bar lengths ( $L_0 \approx 91$  mm,  $L_1 \approx 46$  mm,  $L_2 \approx 20$  mm) except for SFG<sub>3</sub><sup>9.8</sup>(0.493), of which, its geometry is made identical to the fractal insert numerically optimised by Hoi et al. (2019a) with  $L_0 = 77$  mm. On the other hand, the first to the third iterative lateral bar thicknesses ( $t_0$ ,  $t_1$  and  $t_2$ ) are altered to individually vary the  $N$ ,  $t_r$  and  $\sigma$  of the SFGs while keeping the other two parameters constant. The three cases investigated in the present study include: (i) different  $N$  with fixed  $t_r$  and  $\sigma$  ( $N = 1, 2, 3$ ;  $t_r = 6.5$ ;  $\sigma = 0.493$ ), (ii) different  $t_r$  with fixed  $N$  and  $\sigma$  ( $t_r = 4.0, 6.5, 9.8$ ;  $N = 3$ ;  $\sigma = 0.493$ ) and (iii) different  $\sigma$  with fixed  $N$  and  $t_r$  ( $\sigma = 0.270, 0.382, 0.493$ ;  $N = 3$ ;  $t_r = 6.5$ ).

**Table 1** Geometrical parameters of the grids

Parameter	SSG(0.493)	SFG <sub>2</sub> <sup>6.5</sup> (0.493)	SFG <sub>3</sub> <sup>6.5</sup> (0.493)	SFG <sub>3</sub> <sup>6.5</sup> (0.382)	SFG <sub>3</sub> <sup>6.5</sup> (0.270)	SFG <sub>3</sub> <sup>4.0</sup> (0.493)	SFG <sub>3</sub> <sup>9.8</sup> (0.493)	RG(0.492)
$L_0$ (mm)	91.3	91.3	91.3	91.7	92.1	91.0	77.0	20.0
$L_1$ (mm)		45.7	45.7	45.9	46.0	45.5	45.7	
$L_2$ (mm)			20.3	20.4	20.5	20.3	20.4	
$t_0$ (mm)	34.5	28.5	17.5	13.2	9.1	13.3	24.4	5.8
$t_1$ (mm)		4.4	5.4	4.1	2.8	6.7	5.0	
$t_2$ (mm)			2.7	2.0	1.4	3.4	2.5	
$x_*$ (mm)	241.6	292.5	476.0	637.8	932.1	621.9	243.0	69.6
$A_o$ (mm <sup>2</sup> )	3226	3642	4079	5040	6048	4262	2354	203

## 2.2 Experimental Setup and Procedure

Experiments are performed in the same transparent acrylic wind tunnel with the same setup as that in Lee et al. (2021) study. Figure 2 shows the schematic of the experimental setup. The tunnel is 4.41 m in length and has a cross-section of 0.160 m × 0.160 m. Flow straighteners are placed at the inlet right after the bellmouth and in front of the axial draw-through fan (Kruger MTD200, SG) at the outlet. The centreline air inlet velocity is fixed at  $v_{in} = 4$  m/s with hydraulic diameter-based flow Reynolds number  $Re_{D_h} = 4.1 \times 10^4$ . Each turbulence-generating grid is inserted at 2.02 m from the inlet.

A unimorph piezoelectric thin-film (TE Connectivity LDT1-028K, CH), which consists of a PVDF film laminated to a Mylar sheet is cantilevered and placed parallel to the flow. Table 2 tabulates the properties of the piezoelectric cantilever beam (Measurement Specialties 1999, 2015; Danesh-Yazdi et al. 2016; Lee et al. 2021). With the piezoelectric output connected to a 10 MΩ external electrical load, the voltage signal is sampled and digitised for a period of 60 s at a sampling rate of 10<sup>3</sup> Hz using a data acquisition device (LabJack U3-HV, US) with a voltage resolution of 4.88 mV/bit. Under the illumination of an LED light source, the lateral fluctuations of the thin-film, which is fluorescently highlighted at the edges are simultaneously captured for 10 s using an industrial high-speed camera (fps4000-720, UK). The images are recorded at a rate of 10<sup>3</sup> fps with a pixel resolution of 1280 × 720. A simple LED circuit (Fig. 2b) (Lee et al. 2021) is also employed to ensure synchronised measurement of the voltage signal and piezoelectric undulation. For each of the grid investigated, the thin-film is positioned along the grid's centreline at different grid-film distances:  $20 \leq x \leq 400$  mm corresponding to  $0.13 \leq x/D_h \leq 2.50$ , where  $D_h = 160$  mm is the hydraulic diameter of the wind tunnel. The experiment is repeated six times for each  $x/D_h$  to ensure experimental repeatability. Finally, the local centreline mean velocities in  $x$ ,  $y$  and  $z$ -directions at  $x_{peak}$  and  $x/D_h = 0.13$  and 2.50 are measured using a hotwire anemometer (Testo 405i, DE) of accuracy  $\pm 0.3$  m/s. The hand-held probe is first inserted vertically into the wind tunnel along the  $y$ -axis with its sensor head facing the streamwise air flow to measure the instantaneous longitudinal velocity ( $U_{x,ins}$ ). After the probe is rotated 90° for instantaneous spanwise velocity ( $U_{z,ins}$ ) measurement, it is inserted horizontally along the  $z$ -axis to measure the instantaneous vertical velocity ( $U_{y,ins}$ ). For each velocity component, three repeated measurements are performed, and for each measurement the data is logged for a period of 60 s to obtain its time average velocity.

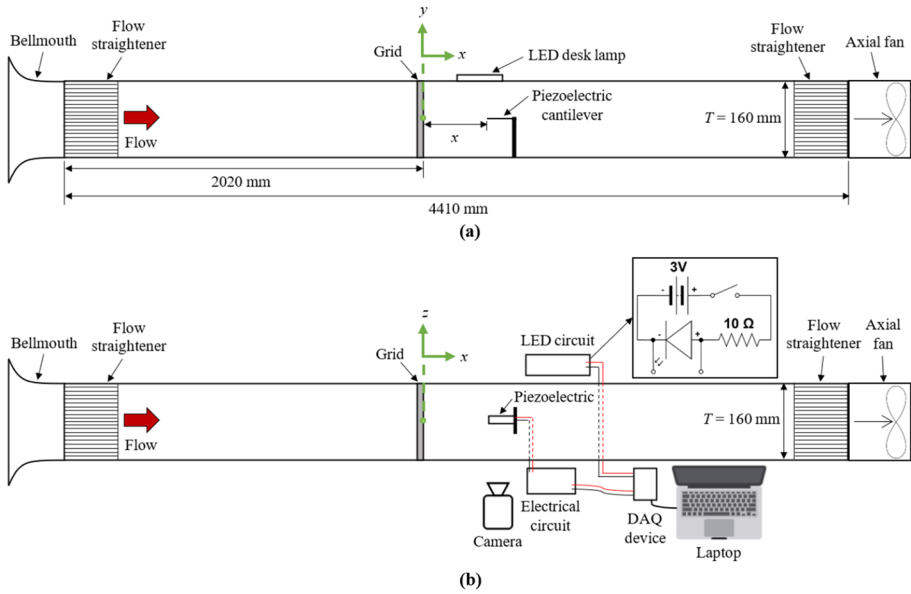


Fig. 2 Schematic of **a** side-view and **b** top-view of the experimental setup

**Table 2** Properties of the piezoelectric cantilever beam (Measurement Specialties 1999, 2015; Danesh-Yazdi et al. 2016; Lee et al. 2021)

Parameter	Symbol	Value
Length (mm)	$l$	32 <sup>[m]</sup>
	$l_p$	30
Width (mm)	$b$	16 <sup>[m]</sup>
	$b_p$	12
Thickness (mm)	$h$	0.22 <sup>[m]</sup>
	$h_p$	0.028
Young’s modulus (N/m <sup>2</sup> )	$E_s$	3.79 × 10 <sup>9</sup>
	$E_p$	3 × 10 <sup>9</sup>
Density (kg/m <sup>3</sup> )	$\rho_s$	1390
	$\rho_p$	1780
Capacitance (nF)	$C$	1.38
Mass (g)	$m$	0.17 <sup>[m]</sup>
Stiffness (N/m)	$k$	17.31 <sup>[c]</sup>
Damping (10 <sup>-3</sup> Ns/m)	$c$	1.87–10.3 <sup>[c]</sup>
Electromechanical coupling coefficient (10 <sup>-6</sup> C/m)	$\theta$	7.69 <sup>[c]</sup>
Natural frequency (Hz)	$f_n$	50.78 <sup>[m]</sup>
Damping ratio (10 <sup>-2</sup> )	$\zeta$	1.72–9.48 <sup>[c]</sup>

Subscript *p* represents PVDF film; subscript *s* the Mylar substrate. Superscript [m] denotes experimentally measured and [c] the calculated values

The piezoelectric thin-film tip deflection  $\delta$  is determined from the experimentally recorded images using the previously developed Thin-Film Fluctuating Image-Detection Algorithm (Lee et al. 2021). The  $\delta$  detected has an average uncertainty of 0.02 mm. The signal-to-noise ratio of  $\delta$  is 4.5 for small amplitude fluctuation, which is  $7.4\times$  lower than the voltage signal-to-electrical noise ratio. The local equivalent lateral flow velocity fluctuation  $v'$  is then calculated from the time derivative of  $\delta$ , i.e.,  $\frac{d\delta}{dt}$  prior to evaluating the corresponding turbulence statistics and induced forcing in the following section. It is worthwhile to mention that when  $v_{in}=5.3$  m/s (viz. the maximum  $v_{in}$  in the absence of a turbulence-generating grid), the piezoelectric thin-film positioned at  $x/D_h=0.56$  on the centreline of the test section without grids has RMS voltage  $V_{rms}=0.18$  V and RMS tip deflection  $\delta_{rms}=0.09$  mm. Such inconsiderable thin-film response signifies that the wind tunnel has a rather low background turbulence.

### 3 Results and Discussion

#### 3.1 Effects of Fractal Iteration $N$ on Centreline Streamwise Flow Characteristics

The experimentally recorded RMS voltage  $V_{rms}$  and RMS tip deflection  $\delta_{rms}$  of the piezoelectric thin-film, as well as their corresponding dominant frequencies  $f_v$  and  $f_\delta$  at different streamwise distances  $x/D_h$  along the centreline of four high  $\sigma$  (0.493) inserts: SSG, SFG<sub>2</sub> ( $N=2$ ) and SFG<sub>3</sub> ( $N=3$ ) with  $t_r=6.5$ , and RG are presented in Fig. 3a and b. The centreline streamwise evolution of the equivalent lateral integral length scale  $L_v$  normalised against the tunnel width  $T$  is plotted in Fig. 3d to determine the size of the large-scale energy-containing eddies generated by the inserts.  $L_v$  is evaluated from Eq. 3 via integrating the autocorrelation function of  $v'$  with respect to time-lapse  $\Delta$  up to the first zero-crossing time  $\tau_{zc}$  of the autocorrelation plot.

$$L_v = v_{in} \int_0^{\tau_{zc}} \frac{\langle v'_t v'_{t+\Delta} \rangle}{\langle v'^2 \rangle} d\Delta \quad (3)$$

As seen in Fig. 3a, the  $V_{rms}$  and  $\delta_{rms}$  induced by SSG and SFG-generated turbulence exhibit a similar profile as described in literature (Hurst and Vassilicos 2007; Mazellier and Vassilicos 2010; Melina et al. 2016). The  $V_{rms}$  and  $\delta_{rms}$  in the turbulence generation region of SSG, SFG<sub>2</sub> and SFG<sub>3</sub> increase, respectively, to a peak at  $x_{peak}/D_h=1.0$ , 1.2 and 1.0 before decreasing exponentially further downstream in the decay region. As for the RG, a power-law decay is observed throughout the entire streamwise distances. Once the SFG-generated flow is fully recovered from the inhomogeneity of the near-field at region adequately far from the grid, it is anticipated that the SFG-induced  $V_{rms}$  and  $\delta_{rms}$  will also undergo a power-law decay if the experiments were to be conducted further downstream in the decay region ( $x/D_h > 2.5$ ) as supported by the studies conducted by Hearst and Lavoie (2014, 2016). In view of the fact that the magnitude of the turbulence intensity peak is proportional to the  $t_0/L_0$  ratio of SFG (Gomes-Fernandes et al. 2012), the  $V_{rms}$  and  $\delta_{rms}$  peaks are the most prominent for SSG, with values of 7.6 V and 3.1 mm, which are about  $2\times$ ,  $3\times$  and  $9\times$  larger than SFG<sub>2</sub>, SFG<sub>3</sub> and RG, respectively. SSG has an earlier peak point than SFG<sub>2</sub> as a result of its smaller wake-interaction length scale  $x_*$ , which represents the location on the centreline where the wakes from the largest grid bars interact, bounding the  $x_{peak}$  (Mazellier and Vassilicos 2010). However, due to the large  $t_0/L_0$  ratio of SSG (0.38) and SFG<sub>2</sub> (0.31), their  $x_{peak}$  are larger than expected despite having a smaller  $x_*$  than SFG<sub>3</sub>.



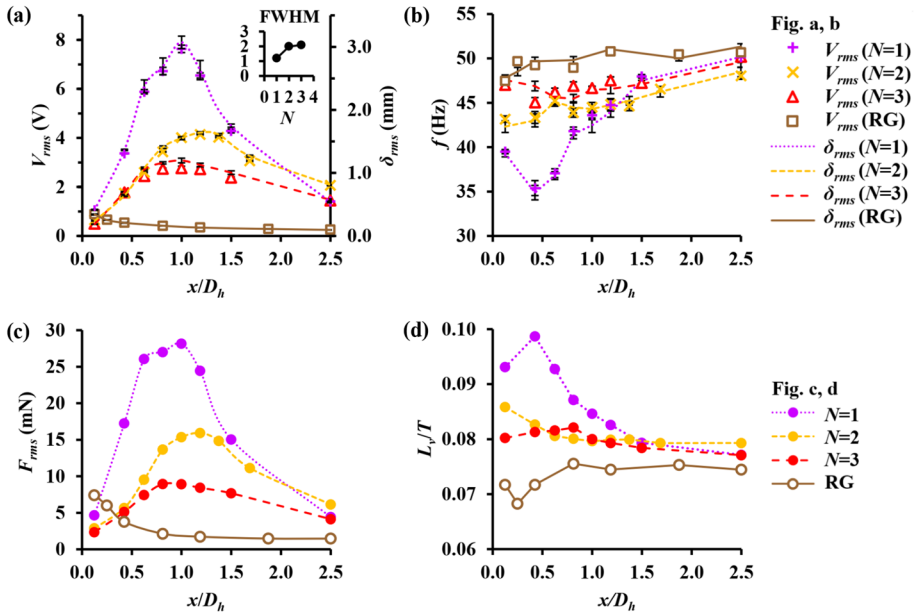


**Fig. 3** **a** RMS of experimentally recorded piezoelectric output voltage  $V_{rms}$  and tip deflection  $\delta_{rms}$  [top right shows the full width at half maximum (FWHM) of the respective peaks], as well as **b** the dominant frequency of voltage signal  $f_V$  and thin-film flapping  $f_\delta$  at different streamwise distances  $x/D_h$  along the centreline of SSG(0.493), SFG<sub>2</sub><sup>6.5</sup>(0.493), SFG<sub>3</sub><sup>6.5</sup>(0.493) and RG(0.492) [Symbol: piezoelectric measurement; Line: camera detection]; with the corresponding grid-induced **c** RMS excitation force acting on the piezoelectric thin-film  $F_{rms}$ , and **d** equivalent lateral integral length scale  $L_v/T$  against  $x/D_h$

The reason is that a thick first iteration grid bar not only leads to smaller  $A_o$ , which intensifies the contraction effect to further accelerate the flow, but also enlarges the size of the recirculation regions immediately in the lee of the largest bar, and consequently diverges the streamlines of the flow towards the tunnel walls (Laizet and Vassilicos 2011). Hence, the wakes from the largest bar tend to meet further downstream and cause a delay in wake-interaction. In addition, an increase in  $x_*$  creates an extended turbulence generation region, giving rise to an increase in the full width at half maximum (FWHM) of the peaks with increasing  $N$ . Nevertheless, the FWHM of the peaks for SFG<sub>2</sub> is slightly higher than anticipated due to the aforementioned wake-interaction-delay.

As shown in Fig. 3b, there is a general increase in the  $f_V$  and  $f_\delta$  trends with increasing  $x/D_h$  for all inserts, of which, the  $L_v/T$  profiles in Fig. 3d are virtually a reverse of the thin-film response dominant frequencies  $f$  profiles. Without the addition of smaller scale bars, the SSG-generated flow, particularly in the domain proximate to grid ( $x/D_h \leq 0.6$ ) is mainly dominated by the considerably large-scale ( $14 \text{ mm} < L_v < 16 \text{ mm}$ ), low-frequency ( $35 \text{ Hz} < f < 40 \text{ Hz}$ ) eddies generated from the thick square bar, which evolve into smaller ones as proceeding downstream. With constant  $t_r$  (for the case of SFG) and  $\sigma$ ,  $t_0$  increases as a function of decreasing  $N$ . The overall  $f$  is therefore the lowest for SSG followed by SFG<sub>2</sub>, SFG<sub>3</sub> and RG owing to the slowly rotating, larger  $L_v/T$  vortices shed from the thicker first iteration grid bar, which act as the primary flow components in inducing thin-film flapping. When additional fractal scales are added to the grid, energy are re-distributed to a broader range of scales in the flow (Nedić et al. 2015). The presence of higher frequency,

small-sized eddies could lead to less potent flow structures driving the thin-film fluctuations, thus an overall lower  $V_{rms}$  and  $\delta_{rms}$  detected for higher  $N$  grid (Fig. 3a).

Figure 3c compares the centreline RMS turbulence-induced excitation force  $F_{rms}$  acting on the thin-film (turbulence forcing) in the lee of RG and SFGs of different  $N$ . The time-dependent normal flow excitation force  $F_y$  is calculated from the following equation (Sodano et al. 2004; Elvin et al. 2006),

$$m\ddot{\delta} + c\dot{\delta} + k\delta - \vartheta V = F_y \quad (4)$$

where  $\vartheta$  is the electromechanical coupling coefficient,  $m$ ,  $c$  and  $k$  are the mass, damping and stiffness of the piezoelectric beam. These parameters are determined using the same approach as our previous study (Lee et al. 2021) and are listed in Table 2. The  $F_{rms}$  calculated for all inserts display a similar streamwise evolution as the  $V_{rms}$  and  $\delta_{rms}$  in Fig. 3a with only a minute shift in the  $x_{peak}$  of SFG<sub>3</sub>. As high as 28 mN is secured from the SSG-generated flow at the  $x_{peak}$ , followed by the flow generated from SFG<sub>2</sub> (16 mN), SFG<sub>3</sub> (9 mN) and RG (7 mN). Interestingly, in spite of the lower  $V_{rms}$  and  $\delta_{rms}$  induced by RG-generated turbulence in comparison to SSG at  $x/D_h=0.13$ , SFG<sub>2</sub> and SFG<sub>3</sub> at  $x/D_h=0.25$ , the  $F_{rms}$  for RG is larger than the three grids at the respective locations. This is the consequence of the additional forcing provided by the small-scale turbulence as supported by the energy spectra  $E_v$  in Fig. 6, of which, the minor peak  $E_v$  (as indicated by the red arrow) of RG is an order of magnitude higher than SSG at  $x/D_h=0.13$  and (SFG<sub>2</sub>, SFG<sub>3</sub>) at  $x/D_h=0.25$ . This result is in line with Lee et al. (2021) finding where the  $F_{rms}$  calculated takes into account the broad-band random forcing across various eddy sizes including those small-scale eddies of higher frequencies, whereas  $V_{rms}$  and  $\delta_{rms}$  merely reflect the vortex shedding intensity of the dominant large eddies.

### 3.2 Effects of Fractal Thickness Ratio $t_r$ on Centreline Streamwise Flow Characteristics

Figure 4a–d show the  $V_{rms}$  and  $\delta_{rms}$ ,  $f$ ,  $F_{rms}$  and  $L_v/T$  against  $x/D_h$  along the centreline of three SFGs ( $N=3$ ,  $\sigma=0.493$ ) of different  $t_r$ . All inserts demonstrate an increase in  $V_{rms}$ ,  $\delta_{rms}$  and  $F_{rms}$  with  $x/D_h$  followed by an exponential decay beyond the peak (Fig. 4a, c). The  $V_{rms}$ ,  $\delta_{rms}$  and  $F_{rms}$  of SFG<sup>9.8</sup> at  $x_{peak}/D_h=0.8$  are  $1.5\times$  to  $1.6\times$  higher than SFG<sup>6.5</sup> at  $x_{peak}/D_h=1.0$ , and  $1.6\times$  to  $1.7\times$  higher in comparison with SFG<sup>4.0</sup> at  $x_{peak}/D_h=1.2$ . This is consonant with the results reported in literature (Hurst and Vassilicos 2007; Mazellier and Vassilicos 2010) where turbulence intensity heightens and  $x_{peak}$  shortens when increasing  $t_r$ . The decrease in  $x_*$  with  $t_r$  brings about a decrease in both  $x_{peak}/D_h$  and FWHM of the peaks. By keeping the  $\sigma$  and  $N$  of the grid constant, first iteration bar thickens while second and third iteration bars thinned when increasing  $t_r$ , giving rise to a wider range of eddy's scale in the flow. As depicted in Fig. 4b, d, the vortical structures generated from SFG<sup>9.8</sup> with large  $t_0/L_0$  ratio (0.32) are relatively low in frequency ( $f \approx 40$  Hz) and large in size ( $L_v \approx 15$  mm) in the region very close to the grid. For all three inserts, we once again notice a general increase in  $f$  and decrease in  $L_v/T$  with increasing  $x/D_h$ .

The  $V_{rms}$ ,  $\delta_{rms}$  and  $F_{rms}$  in Fig. 4a, c are greater for higher  $t_r$  grid in the turbulence generation region as a consequence of the larger size energy-containing eddies generated from the thicker first iteration bar. However, the  $V_{rms}$ ,  $\delta_{rms}$  and  $F_{rms}$  for all three inserts coincide to almost similar values in the decay region, whereby at  $x/D_h=2.5$ , the values are the largest for SFG<sup>4.0</sup> and the lowest for SFG<sup>9.8</sup>. This could be explained by the higher energy dissipation rate experienced by larger  $t_r$  grid as evidenced in Fig. 6, where both

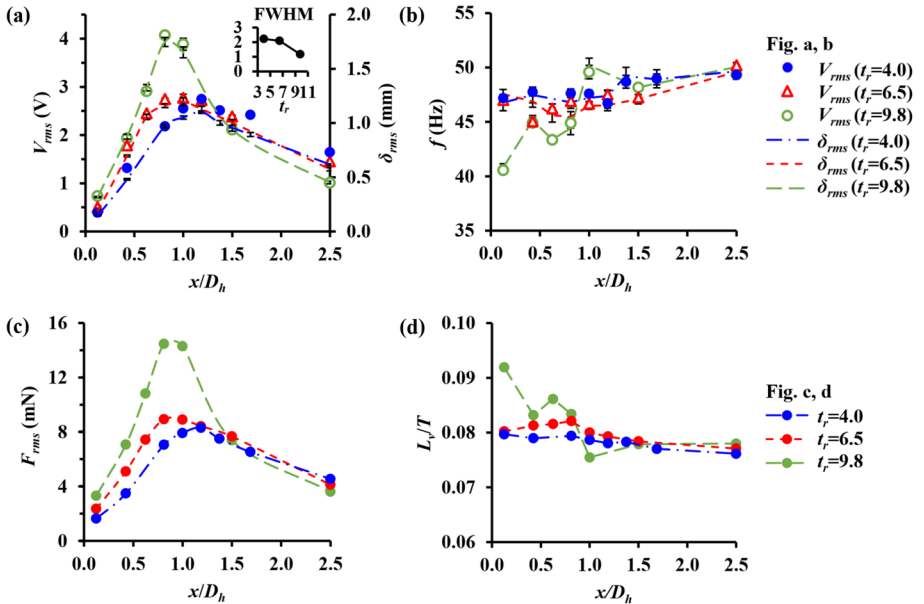


**Fig. 4** Downstream evolution of **a**  $V_{rms}$  (symbol) and  $\delta_{rms}$  (line), **b**  $f_V$  (symbol) and  $f_\delta$  (line), **c**  $F_{rms}$  and **d**  $L_v/T$  along the centreline of SFG $_{3.0}^{4.0}$  (0.493), SFG $_{3.5}^{6.5}$  (0.493) and SFG $_{3.8}^{9.8}$  (0.493)

major and minor peaks’ intensities in the decay region of SFG $^{9.8}$  attenuate 3× and 4× faster than SFG $^{6.5}$  and SFG $^{4.0}$ , respectively. Considering that smallest eddies decay the fastest, the finer small-scale structures present in higher Reynolds number flow (Davidson 2004) generated along the centreline of smaller  $A_o$  grid, as well as the smaller size vortices shed from the thinner second and third iteration bars, may have prompted the energy dissipation rate to increase with  $t_r$  in the decay region.

### 3.3 Effects of Blockage Ratio $\sigma$ on Centreline Streamwise Flow Characteristics

Figure 5a–d illustrate the downstream profile of the centreline  $V_{rms}$  and  $\delta_{rms}$ ,  $f$ ,  $F_{rms}$  and  $L_v/T$  leeward of three different  $\sigma$  SFGs with  $N=3$  and  $t_r=6.5$ . The  $V_{rms}$ ,  $\delta_{rms}$  and  $F_{rms}$  for all the three inserts in Fig. 5a, c demonstrate turbulence generation and decay albeit with a slightly irregular trend detected for SFG(0.270)’s  $F_{rms}$  distribution. SFG(0.493) has peak  $V_{rms}$ ,  $\delta_{rms}$  and  $F_{rms}$  that are approximately 2× larger than SFG(0.382) and 3 to 5× larger than SFG(0.270). The peak location is further and the FWHM is wider when reducing  $\sigma$ . This again is the result of larger  $x_s$  owing to the smaller  $t_0$  of a lower-blockage SFG and therefore, a flatter peak is attained for SFG(0.270).

In view of the increase in all three iterations lateral bar thickness with  $\sigma$ , the multi-scale jets produced from the smaller openings are accelerated. Moreover, there is an overall decrease in  $f$  and increase in size ( $L_v/T$ ) of the multilength-scale turbulent eddies generated from higher  $\sigma$  grid at each  $x/D_h$  (Fig. 5b, d), giving rise to more effective (energy-containing) flow structures exciting the thin-film flapping. Unlike the variation in  $f$  and  $L_v/T$  with respect to  $x/D_h$  observed for the previous two cases, the  $f$  and  $L_v/T$  for SFG(0.382) and SFG(0.270) are rather constant throughout the entire streamwise distances investigated.

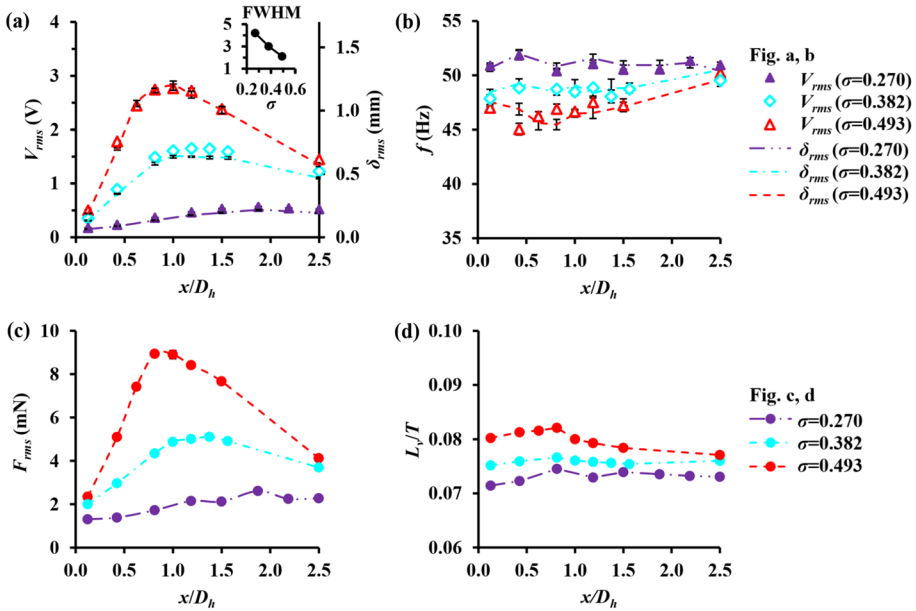


**Fig. 5** **a**  $V_{rms}$  (symbol) and  $\delta_{rms}$  (line), **b**  $f_V$  (symbol) and  $f_\delta$  (line), **c**  $F_{rms}$  and **d**  $L_v/T$  vs.  $x/D_h$  along the centreline of  $SFG_3^{6.5}$  (0.270),  $SFG_3^{6.5}$  (0.382) and  $SFG_3^{6.5}$  (0.493)

This suggests that turbulence generated from low- and medium-blockage SFGs have a higher degree of homogeneity compared to high-blockage SFGs.

### 3.4 Energy Spectra

Figure 6a presents the centreline streamwise 3D energy spectra  $E_v$  of all eight inserts determined from the Fourier transformations of the  $v'$  autocovariance function while Fig. 6b shows the top view of the respective spectra. For each  $x/D_h$  in Fig. 6a, the major peak appearing at frequency  $f$  close to the first resonant mode of piezoelectric beam, which was also observed by Laizet et al. (2015) in the longitudinal energy spectra for SFG, Isaza et al. (2014) for RG and Melina et al. (2016) for SSG, is the result of vortex shedding from the grid bars (Gomes-Fernandes et al. 2015; Melina et al. 2016; Nagata et al. 2017). These equivalent vortex shedding frequencies are in excellent agreement with the  $f_V$  and  $f_\delta$  in Figs. 3b, 4b and 5b. The high vortex shedding intensity observed in the turbulence generation region intensifies with  $t_r$  and  $\sigma$  but weakens with  $N$ , which is identical to the results in Fig. 7a. The shedding effect is the most pronounced for SSG since it has the largest  $t_\theta$ . The major peak  $E_v$  ( $E_{v,max}$ ) at  $x_{peak}/D_h$  leeward of SSG is approximately 2× and 40× higher than  $SFG_3^{9.8}$  (0.493) and RG, respectively. One can also infer that the more intense the vortex shedding, the higher the equivalent vortex shedding energy as represented by the broader  $f$  range of high energy fluctuations with  $E_v > 10^{-4}$  (Fig. 6b). Consequently, more energetic flow fluctuations inducing the thin-film vibration, yielding larger  $\delta_{rms}$  and  $V_{rms}$ .

On the contrary, minor peaks with relatively smaller  $E_v$  tend to occur at higher  $f$  ( $200 \text{ Hz} < f < 350 \text{ Hz}$ ) associated to the second vibration mode of the piezoelectric beam. These minor peaks are the most prominent for RG especially in the region near to grid,

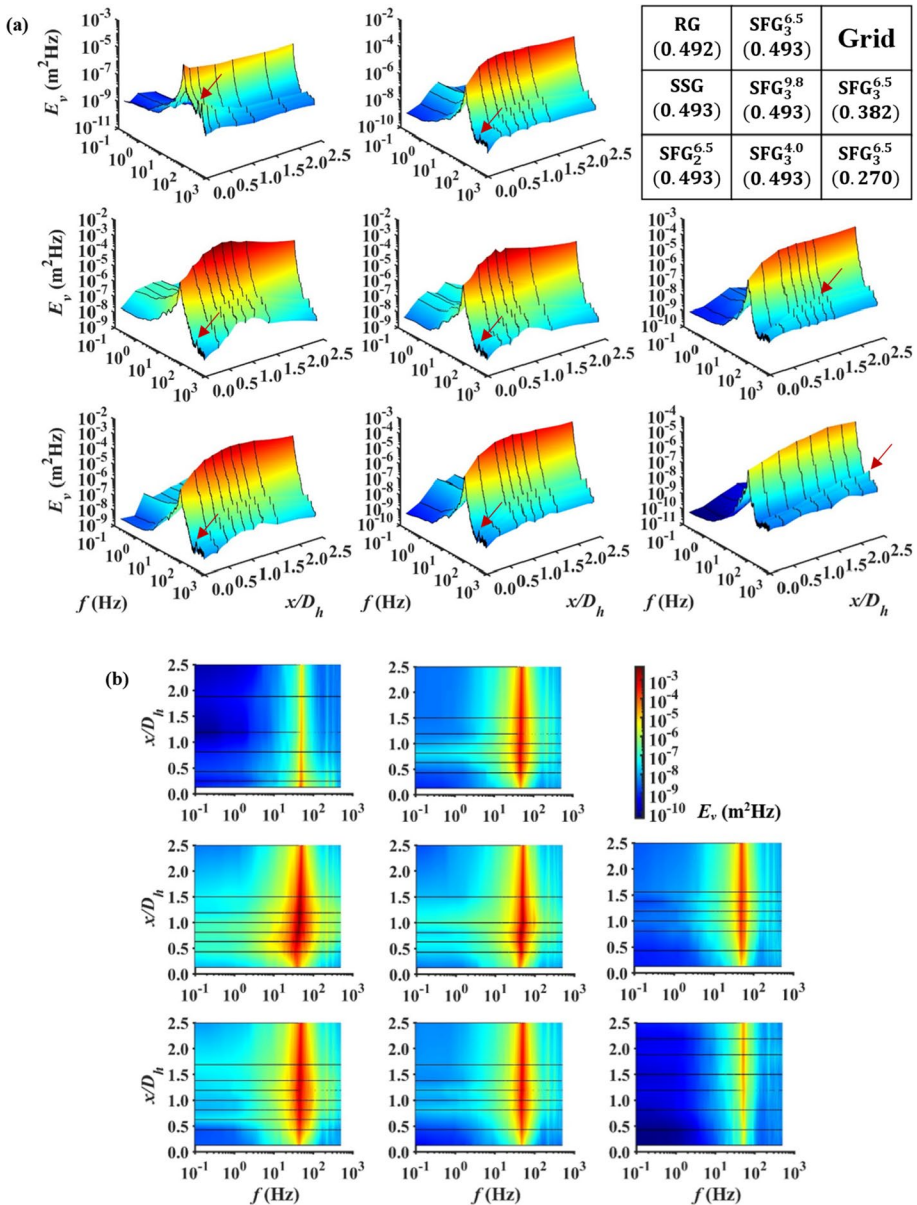


**Fig. 6** **a** Downstream evolution of the centreline energy spectra for all grids; **b** top view of the respective spectra

signifying that higher frequency small-scale eddies possess more significant contribution to RG-induced turbulence when compared to SFG and SSG. Moreover, it is noteworthy that the slight shift in SFG<sub>3</sub><sup>6.5</sup> (0.382)  $F_{rms}$  peak location from  $x/D_h = 1.2$  to  $x/D_h = 1.4$  (Fig. 5c) could be due to the additional forcing provided by the small-scale eddies, given that the minor peak  $E_v$  at  $x/D_h = 1.4$  is  $1.3\times$  higher than at  $x/D_h = 1.2$  albeit the former has a

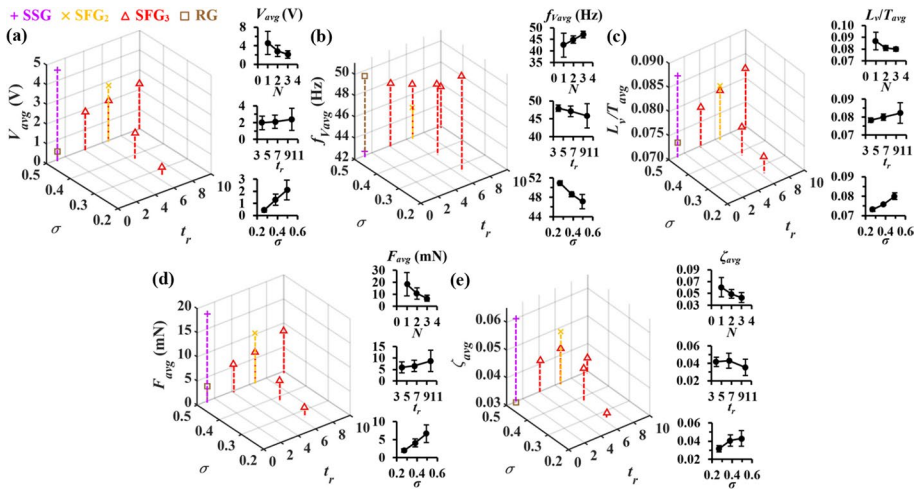


**Fig. 7** a Average  $V_{rms}$ , b  $f_v$ , c  $L_v/T$ , d  $F_{rms}$  and e damping ratio  $\zeta$  downstream of the grids centreline as functions of  $N$ ,  $t_r$  and  $\sigma$

major peak  $E_v$  that is  $1.1\times$  lower than the latter. Last but not least, the streamwise evolution of the  $E_{v,max}$  for all inserts are consistent with the streamwise profiles previously secured for  $V_{rms}$  and  $\delta_{rms}$  in Figs. 3a, 4a and 5a. Both the major and minor peaks in the decay region diminish as one proceeds downstream owing to energy dissipation.

### 3.5 Interplays Between $N$ , $t_r$ and $\sigma$ on the Overall Flow Mechanical Characteristics

Figure 7a–e plot the average  $V_{rms}$  ( $V_{avg}$ ),  $f_v$  ( $f_{Vavg}$ ),  $L_v/T$  ( $L_v/T_{avg}$ ),  $F_{rms}$  ( $F_{avg}$ ) and damping ratio  $\zeta$  ( $\zeta_{avg}$ ) downstream of the grids' centreline against  $N$ ,  $t_r$  and  $\sigma$ . It is immediately apparent from Fig. 7a–c that the  $V_{avg}$  and  $L_v/T_{avg}$  increase with  $t_r$  and  $\sigma$  but decrease with  $N$ , in contrast to  $f_{Vavg}$ . This is attributable to the higher shedding intensity of lower frequency, larger scale energy-containing vortices from the thicker first iteration bar as evidenced in Figs. 6, 7b and c. The  $F_{avg}$  calculated in Fig. 7d ranges from 2.0 to 18.4 mN and exhibits a similar trend as  $V_{avg}$  with respect to  $N$ ,  $t_r$  and  $\sigma$ , denoting that increasing turbulence-induced excitation force acting on the thin-film is generally accompanied by an increase in  $\delta$  and  $V$ . One can also deduce that larger  $V$  signifies larger  $L_v$ , but lower frequency eddies present in the flow. In the context of energy harvesting for vortex-induced vibration-based devices where potent flow fluctuation strength and induced forcing are highly desirable, SFG<sub>3</sub><sup>0.8</sup>(0.493) with considerable  $V_{avg}$  and  $F_{avg}$  turns out to be the best performing grid among all the  $N=3$  SFGs, followed by SFG<sub>3</sub><sup>5.3</sup>(0.493). Thus, despite the fact that the turbulent flow generated by high-blockage grid would become unstable and is less likely to be homogeneous (Corrsin 1963), the turbulence induced by SFG with higher  $\sigma$  is proven in our current work to be favourable for piezoelectric energy harvesting application. The  $V_{avg}$  (4.6 V),  $L_{vavg}$  (13.9 mm) and  $F_{avg}$  (18.4 mN) are the highest while  $f_{Vavg}$  (42.5 Hz) is the lowest in SSG-induced turbulence, of which, the  $V_{avg}$  and  $F_{avg}$  for SSG are twice of SFG<sub>3</sub><sup>0.8</sup>(0.493), and (9×, 5×) higher than the RG, respectively. All the SFGs investigated demonstrate superior flow fluctuation strength and induced forcing than the RG, which

is consistent with the earlier studies (Laizet and Vassilicos 2011; Ferko et al. 2019b; Lee et al. 2021), except for SFG<sub>3</sub><sup>6.5</sup>(0.270) where its  $V_{avg}$  and  $F_{avg}$  are  $1.2\times$  and  $1.7\times$  lower than RG owing to its  $1.8\times$  lower  $\sigma$  than the latter.

In spite of the  $f_{V_{avg}}$  variation with respect to grid geometry, the piezoelectric beam positioned in the lee of all eight inserts vibrates with variations of less than 30% from its own natural frequency  $f_n$ , denoting that  $f_V$  and  $f_\delta$  are associated to the  $f_n$  of piezoelectric beam amalgamate with the characteristic frequencies of vortices shed from the multi-scale grid bars. It is observed in Fig. 7c that the  $L_v/T_{avg}$  gradient between  $N=2$  and 3 is less steep than that of  $N=1$  and 2. Notwithstanding the fact that the increase in  $L_v/T_{avg}$  when  $N$  decreases from 3 to 2 is the result of larger  $t_0$  as well as the removal of the third iteration bar, the thinner second iteration bar of SFG<sub>2</sub><sup>6.5</sup>(0.493) compared to SFG<sub>3</sub><sup>6.5</sup>(0.493) would offset the  $L_v/T_{avg}$  increment to a certain extent. This implies that the  $L_v$  calculated in the present study ( $10.9\text{ mm} < L_v < 15.8\text{ mm}$ ) is essentially affected by  $t_0$ , yet the size of the eddies generated from higher iteration bars also impose some minor effect on the  $L_v$ . Given that the whiskers in the line plots represent the standard deviation of the values over the entire streamwise distances investigated, the extremely large whiskers observed for SSG and SFG<sub>3</sub><sup>9.8</sup>(0.493) could be an indication of the highly inhomogeneous flow generated.

Based on Lee et al. (2021) finding, the possible causes for the high  $\zeta$  attained along the centreline leeward of SFG are (i) the high velocity jet flowing through the central opening, which may possibly hinder the up and down movement of the thin-film, and (ii) the multilength-scale flow structures generated, which makes the fluid domain around the thin-film to become rather crowded. Hence, the flow generated from RG of uniform geometry has the lowest  $\zeta_{avg}$  among the grids (Fig. 7e). In addition, one can also infer that the smaller the central opening (larger  $t_0$ ), the stronger the central jet as a result of contraction effect, thereby higher  $\zeta_{avg}$ . Although at first glance, the  $\zeta_{avg}$  seems to have the same trend as  $V_{avg}$ ,  $L_v/T_{avg}$  and  $F_{avg}$ , the  $\zeta_{avg}$  for SFG<sub>3</sub><sup>9.8</sup>(0.493) is rather low despite having larger  $t_0$ . This could be due to its smaller  $L_0$  and its asymmetrical fractal geometry in comparison to other SFGs, where the absence of vortices shed from the second iteration bar at the central opening (Fig. 1g) may have prompted the local multilength-scale flow domain to be less crowded, and subsequently lower  $\zeta_{avg}$ . For the case of different  $\sigma$ , the  $\zeta_{avg}$  for  $\sigma=0.270$  and  $\sigma=0.382$  are slightly above expectation compared to  $\sigma=0.493$ . Unequivocally, the central jet is weaker for lower  $\sigma$  insert with large  $A_o$ , however the thinner second and third iteration bars of SFG<sub>3</sub><sup>6.5</sup>(0.270) and SFG<sub>3</sub><sup>6.5</sup>(0.382) create large number of small-scale disordered eddies in the flow, inducing thin-film damping. It is also important to note that greater  $t_0$  brings about larger sized eddies impinging the thin-film surface, which yields substantial film vibration to overcome the thin-film damping instigated by the stronger central jet. Therefore, we still obtain considerably high  $F_{avg}$  and  $V_{avg}$  albeit with high  $\zeta_{avg}$ .

The local centreline mean velocities  $U$  at  $x/D_h=0.13$ , 2.50 and  $x_{peak}$  of each grid are normalised against  $v_{in}$  ( $U/v_{in}$ ) and plotted in Fig. 8a, where

$$U = \sqrt{U_x^2 + U_y^2 + U_z^2} \tag{5}$$

with  $U_x$ ,  $U_y$  and  $U_z$  denoting respectively, the local centreline mean velocities in  $x$ ,  $y$  and  $z$ -directions measured using hotwire anemometer. The corresponding ratio of the  $U$  gradient in the turbulence decay region to that in the generation region ( $m_d/m_g$ ) are depicted in Fig. 8b.

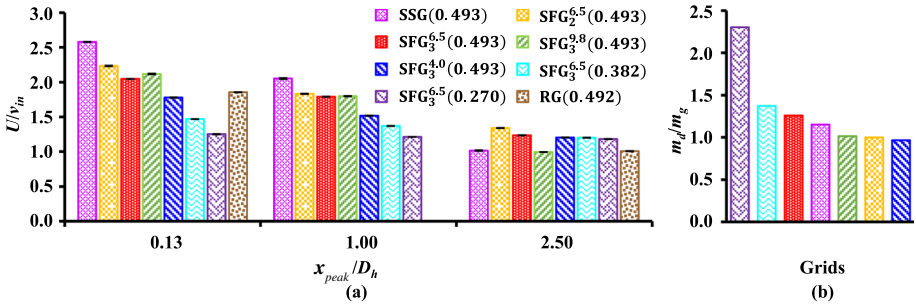


**Fig. 8** **a** Normalised local centreline mean velocity  $U/v_{in}$  at  $x/D_h=0.13, 2.50$  and the peak location  $x_{peak}$  of all grids; **b** the corresponding ratio  $m_d/m_g$  of  $U$  gradient in the turbulence decay region ( $x_{peak} \rightarrow x/D_h=2.50$ ) to that in the generation region ( $x/D_h=0.13 \rightarrow x_{peak}$ )

As shown in Fig. 8a, the centreline jet behind the central opening of all grids at  $x/D_h=0.13$  have  $1.2 < U/v_{in} < 2.6$ , where the  $U$  decreases with  $x/D_h$  towards  $v_{in}$  further downstream. At  $x/D_h=2.5$ , the  $U$  of all SFGs, excluding SFG<sub>3</sub><sup>9.8</sup>(0.493) remain higher than  $v_{in}$  by about 18% to 34% when compared to SSG and RG, which is consonant with the earlier study by Melina et al. (2016). Apart from SFG<sub>3</sub><sup>9.8</sup>(0.493) and RG, the  $U$  at  $x/D_h=0.13$  increases with  $t_0$  in view of the fact that the jet accelerates more rapidly when flowing through smaller sized central opening. In close proximity to the grid, SSG and SFGs with  $t_r \geq 6.5$  have  $U$  that are higher than RG of equivalent  $\sigma$ . The overall  $U$  decrement rate is remarkably high for SSG and SFG<sub>3</sub><sup>9.8</sup>(0.493) with the former having the fastest decrement, SFG<sub>3</sub><sup>6.5</sup>(0.270) the slowest, and RG somewhere in-between. Interestingly, the overall  $U$  decrement rate appears to be interrelated with the FWHM of the  $V_{rms}$  and  $\delta_{rms}$  peaks, namely the slower the  $U$  decrement, the more protracted the turbulence generation region, viz. larger FWHM. As such, the  $U$  decrement rate displays the same trend as those of  $V_{rms}$ ,  $\delta_{rms}$  and  $F_{rms}$ , i.e., increase for larger values of  $t_r$  [in good agreement with the results reported by Hurst and Vassilicos (2007) and Mazellier and Vassilicos (2010)] and  $\sigma$  but smaller  $N$ . These further shed light on the lower  $V_{rms}$ ,  $\delta_{rms}$  and  $F_{rms}$  detected in the decay region when increasing  $t_r$  (Fig. 4a, c).

It is clear from Fig. 8b that the rate where  $U$  declines in the turbulence decay region is comparable to that in the generation region ( $m_d/m_g \approx 1$ ) for SFG<sub>3</sub><sup>4.0</sup>(0.493), SFG<sub>3</sub><sup>9.8</sup>(0.493) and SFG<sub>2</sub><sup>6.5</sup>(0.493). For the remaining grids,  $m_d/m_g$  increases with  $N$  and when  $\sigma$  reduces. This could again be explained by the extended turbulence generation region as a result of larger  $x_*$ , which prompts  $U$  to decline slower in the generation region. Nonetheless, it is worthwhile to note that the last measurement location ( $x/D_h=2.5$ ) may not be adequately far away from the insert to fully capture the  $U$  decrement in the decay region. This is especially true for SFG<sub>3</sub><sup>6.5</sup>(0.270) where the decrease in  $U$  has yet to reach a plateau because of its large  $x_{peak}$ , leading to an exceptionally high  $m_d/m_g$ .

### 3.6 Probability and Frequency Distributions of Piezoelectric Voltage Response

The cumulative probability of centreline  $V^2$  at the  $x_{peak}$  are plotted in Fig. 9a to compare the probability distributions of the random piezoelectric voltage response towards the



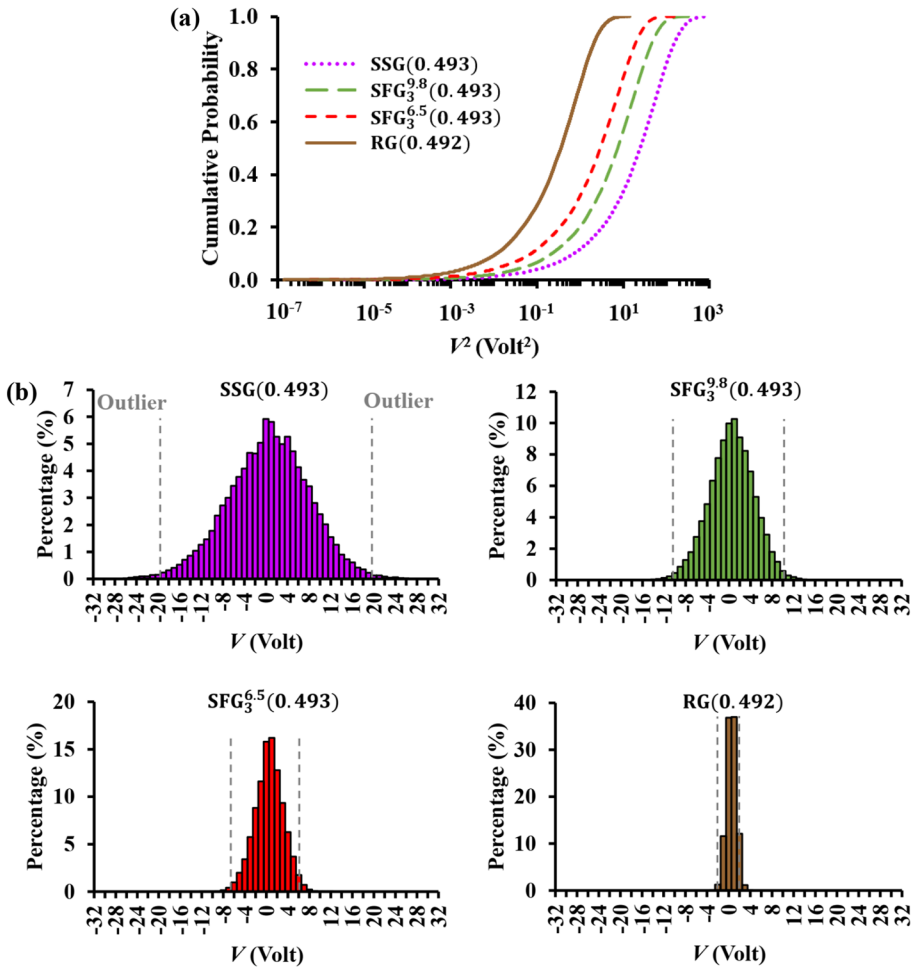


**Fig. 9** a Cumulative probability of centreline  $V^2$  at  $x_{peak}$  of SSG(0.493),  $SFG_3^{9.8}(0.493)$ ,  $SFG_3^{6.5}(0.493)$  and RG(0.492), as well as b the corresponding  $V$  histograms

turbulent flows generated by the best performing grids (grid that generates greatest flow fluctuation strength and turbulence forcing) for different  $N$  (SSG),  $t_r$  [ $SFG_3^{9.8}(0.493)$ ] and  $\sigma$  [ $SFG_3^{6.5}(0.493)$ ] against RG. It is apparent that the grid with larger  $V_{rms}$  and  $\delta_{rms}$  has a higher probability in obtaining large  $V^2$ . SSG has the highest  $V^2$  among the four inserts at  $x_{peak}$ , of which, top 5 percentile have  $V^2 > 225 \text{ V}^2$  while top 1 percentile has  $V^2 > 403 \text{ V}^2$ . This is followed by  $SFG_3^{9.8}(0.493)$  where 95% of  $V^2$  are below  $66 \text{ V}^2$  while top 1 percentile has  $V^2 > 115 \text{ V}^2$ . For  $SFG_3^{6.5}(0.493)$ , 99% of  $V^2$  are not more than  $47 \text{ V}^2$  and this is narrowed down to  $5 \text{ V}^2$  for RG.

In Fig. 9b, we present the centreline  $V$  histograms for the corresponding grids at  $x_{peak}$ . Clearly, the  $V$  induced by all the four inserts are normally distributed. One can see that the voltage response is most often found near zero values and that an increase in the voltage magnitude is generally accompanied by a decrease in the frequency of

occurrence. All histograms are in good agreement with the cumulative probability distributions in Fig. 9a. The frequency in attaining high  $V$  is the rarest for RG with  $V$  ranging between  $-4$  and  $4$  V only. The  $V$  histogram becomes more spread out for similar  $\sigma$  SFG as supported by the wider  $V$  range of SFG<sub>3</sub><sup>6.5</sup>(0.493) ( $-12$  to  $12$  V) and SFG<sub>3</sub><sup>9.8</sup>(0.493) ( $-18$  to  $18$  V) of larger  $t_r$ . Remarkably, the removal of smaller scale bars from the insert causes the histogram for SSG to have the widest  $V$  range ( $-31$  to  $30$  V). All inserts have almost the same percentage of outlier in their respective voltage distributions, ranging from 0.7% (RG) to 1.1% (SSG).

Both the cumulative probability distribution and histogram plots in Fig. 9 reveal the variation of voltage response with respect to grid conformation. The thin-film flapping induced by large  $t_r$  SFG presents higher centreline voltage output over the RG of the same  $\sigma$ , with SSG outperforming the rest. Hence, SSG is deemed a promising turbulator in producing potent turbulence strength flow that is highly desirable for piezoelectric energy harvesting from turbulence-induced vibration.

## 4 Conclusions

The effects of fractal iteration  $N$ , thickness ratio  $t_r$  and blockage ratio  $\sigma$  on the mechanical characteristics of fractal grid-generated turbulence were experimentally explored by means of PTFV. Measurements of the piezoelectric thin-film tip deflection  $\delta$  and voltage response  $V$  at different grid-film distances  $x/D_h$  along the centreline leeward of a SSG and various SFGs revealed increasing flow fluctuation strength in the turbulence generation region followed by a decay further downstream of the grids. Results showed that the distance from the grid where  $V_{rms}$  and  $\delta_{rms}$  peak is a decreasing function of  $\sigma$  and  $t_r$ . An increase in  $N$  along with a decrease in  $t_r$  and  $\sigma$  leads to an elongated turbulence generation region as a result of larger wake-interaction length scale  $x_*$  and slower local centreline mean velocity  $U$  decrement.

In contrast to the average dominant frequency of voltage signal  $f_V$  ( $f_{V_{avg}}$ ), the heighten in the average  $V_{rms}$  ( $V_{avg}$ ), equivalent lateral integral length scale  $L_V/T$  ( $L_V/T_{avg}$ ) and millinewton turbulence forcing  $F_{rms}$  ( $F_{avg}$ ) downstream of the grids' centreline with increasing  $t_r$  and  $\sigma$  but decreasing  $N$  is the consequence of the higher shedding intensity of lower frequency, larger scale energy-containing vortices from the thicker first iteration bar, which acts as the primary flow components in inducing thin-film flapping. For higher  $\sigma$  SFG, the accelerated multi-scale jets produced from the smaller grid openings, in addition to the more energetic vortex shedding from all three iterations bars of greater thickness further promotes the thin-film undulation. However, the higher: energy dissipation rate,  $U$  decrement rate and local deceleration experienced in the decay region of larger  $t_r$  grid give rise to lower  $V_{rms}$ ,  $\delta_{rms}$  and  $F_{rms}$ , particularly in the decay regime of SFG<sub>3</sub><sup>9.8</sup>(0.493). Interestingly, the additional fractal scales of larger  $N$  grid results in less potent, faster rotating, smaller size vortices driving the thin-film vibration.

The flow generated by medium to high-blockage SFGs exhibit greater fluctuation strength and turbulence forcing than the RG, with the ( $V_{avg}$ ,  $F_{avg}$ ) of SSG being twice of the best performing  $N=3$  SFG [i.e., SFG<sub>3</sub><sup>9.8</sup>(0.493)], and ( $9\times$ ,  $5\times$ ) higher than the RG of equivalent  $\sigma$ . Although the high turbulence intensity multilength-scale turbulence generated from the SFG is favourable for turbulent mixing and heat transfer enhancement (Teh et al. 2015; Skanthan et al. 2018; Chew et al. 2022; Hoi et al. 2022), the superior fluctuation strength ( $V_{rms}=7.6$  V,  $\delta_{rms}=3.1$  mm) and turbulence forcing ( $F_{rms}=28$  mN) demonstrated

by the high-blockage SSG-generated flow at  $x_{peak}$  enables SSG to serve as a promising turbulator for fluidic energy harvesting application.

**Author Contributions** TSL conducted the experiments, performed data analysis and prepared the manuscript draft. EHO, WSC and JJF supervised the project, revised and edited the manuscript. All authors reviewed the manuscript.

**Funding** Open Access funding enabled and organized by CAUL and its Member Institutions. This work was financially supported by Monash University Malaysia under the Graduate Research Merit Scholarship Programme (MUM-25034979).

**Availability of Data and Materials** Dataset can be made available from the corresponding authors upon request.

## Declarations

**Conflict of interest** The authors have no competing interests to declare that are relevant to the content of this article.

**Ethical Approval** Not applicable.

**Open Access** This article is licensed under a Creative Commons Attribution 4.0 International License, which permits use, sharing, adaptation, distribution and reproduction in any medium or format, as long as you give appropriate credit to the original author(s) and the source, provide a link to the Creative Commons licence, and indicate if changes were made. The images or other third party material in this article are included in the article's Creative Commons licence, unless indicated otherwise in a credit line to the material. If material is not included in the article's Creative Commons licence and your intended use is not permitted by statutory regulation or exceeds the permitted use, you will need to obtain permission directly from the copyright holder. To view a copy of this licence, visit <http://creativecommons.org/licenses/by/4.0/>.

## References

- Batchelor, G.K., Townsend, A.A.: Decay of vorticity in isotropic turbulence. Proc. R. Soc. Lond. Ser. A **190**(1023), 534–550 (1947). <https://doi.org/10.1098/rspa.1947.0095>
- Chew, S.H., Hoi, S.M., Tran, M.-V., Foo, J.J.: Partially-covered fractal induced turbulence on fins thermal dissipation. Sci. Rep. **12**, 7861 (2022). <https://doi.org/10.1038/s41598-022-11764-x>
- Comte-Bellot, G., Corrsin, S.: The use of a contraction to improve the isotropy of grid-generated turbulence. J. Fluid Mech. **25**(4), 657–682 (1966). <https://doi.org/10.1017/S0022112066000338>
- Corrsin, S.: Turbulence: Experimental Methods. Springer, Berlin (1963)
- Danesh-Yazdi, A.H., Elvin, N., Andreopoulos, Y.: Parametric analysis of fluidic energy harvesters in grid turbulence. J. Intell. Mater. Syst. Struct. **27**(20), 2757–2773 (2016). <https://doi.org/10.1177/1045389X16641207>
- Davidson, P.A.: Turbulence: An Introduction for Scientists and Engineers. OUP Oxford (2004)
- Elvin, N.G., Lajnef, N., Elvin, A.A.: Feasibility of structural monitoring with vibration powered sensors. Smart Mater. Struct. **15**(4), 977–986 (2006). <https://doi.org/10.1088/0964-1726/15/4/011>
- Ferko, K., Lachendro, D., Chiappazzi, N., Danesh-Yazdi, A.H.: Interaction of side-by-side fluidic harvesters in fractal grid-generated turbulence. Proc. SPIE **10595**, 105951E (2018)
- Ferko, K., Chiappazzi, N., Gong, J., Danesh-Yazdi, A.H.: Average power output and the power law: identifying trends in the behavior of fluidic harvesters in grid turbulence. Proc. SPIE **10967**, 109670Z (2019a)
- Ferko, K., Chiappazzi, N., Gong, J., Danesh-Yazdi, A.H.: Power output comparison of side-by-side fluidic harvesters in different types of fractal grid-generated turbulence. Proc. SPIE **10967**, 109670P (2019b)
- Fragner, R., Mazellier, N., Halter, F., Chauveau, C., Gökalp, I.: Multi-scale high intensity turbulence generator applied to a high pressure turbulent burner. Flow Turbul. Combust. **94**(1), 263–283 (2015). <https://doi.org/10.1007/s10494-014-9556-2>

- Geipel, P., Goh, K.H.H., Lindstedt, R.P.: Fractal-generated turbulence in opposed jet flows. *Flow Turbul. Combust.* **85**(3), 397–419 (2010). <https://doi.org/10.1007/s10494-010-9288-x>
- Goh, M.J.S., Chiew, Y.S., Foo, J.J.: Fractal-induced 2D flexible net undulation. *Sci. Rep.* **11**, 7063 (2021). <https://doi.org/10.1038/s41598-021-86418-5>
- Gomes-Fernandes, R., Ganapathisubramani, B., Vassilicos, J.C.: Particle image velocimetry study of fractal-generated turbulence. *J. Fluid Mech.* **711**, 306 (2012). <https://doi.org/10.1017/jfm.2012.394>
- Gomes-Fernandes, R., Ganapathisubramani, B., Vassilicos, J.C.: The energy cascade in near-field non-homogeneous non-isotropic turbulence. *J. Fluid Mech.* **771**, 676 (2015). <https://doi.org/10.1017/jfm.2015.201>
- Guilarte Herrero, A., Noguchi, A., Kusama, K., Shigeta, T., Nagata, T., Nonomura, T., Asai, K.: Effects of compressibility and Reynolds number on the aerodynamics of a simplified corrugated airfoil. *Exp. Fluids* **62**(4), 63 (2021). <https://doi.org/10.1007/s00348-021-03164-0>
- Hearst, R.J., Lavoie, P.: Decay of turbulence generated by a square-fractal-element grid. *J. Fluid Mech.* **741**, 567–584 (2014). <https://doi.org/10.1017/jfm.2013.684>
- Hearst, R.J., Lavoie, P.: Effects of multi-scale and regular grid geometries on decaying turbulence. *J. Fluid Mech.* **803**, 528–555 (2016). <https://doi.org/10.1017/jfm.2016.515>
- Hoi, S.M., Teh, A.L., Ooi, E.H., Chew, I.M.L., Foo, J.J.: Forced convective heat transfer optimization of plate-fin heat sink with insert-induced turbulence. *Appl. Therm. Eng.* **160**, 114066 (2019a). <https://doi.org/10.1016/j.applthermaleng.2019.114066>
- Hoi, S.M., Teh, A.L., Ooi, E.H., Chew, I.M.L., Foo, J.J.: Plate-fin heat sink forced convective heat transfer augmentation with a fractal insert. *Int. J. Therm. Sci.* **142**, 392–406 (2019b). <https://doi.org/10.1016/j.ijthermalsci.2019.04.035>
- Hoi, S.M., Ooi, E.H., Chew, I.M.L., Foo, J.J.: SPTV sheds light on flow dynamics of fractal-induced turbulence over a plate-fin array forced convection. *Sci. Rep.* **12**, 76 (2022). <https://doi.org/10.1038/s41598-021-02872-1>
- Hurst, D., Vassilicos, J.C.: Scalings and decay of fractal-generated turbulence. *Phys. Fluids* **19**(3), 035103 (2007). <https://doi.org/10.1063/1.2676448>
- Isaza, J.C., Salazar, R., Warhaft, Z.: On grid-generated turbulence in the near- and far field regions. *J. Fluid Mech.* **753**, 402–426 (2014). <https://doi.org/10.1017/jfm.2014.375>
- Krogstad, P.Å., Davidson, P.A.: Near-field investigation of turbulence produced by multi-scale grids. *Phys. Fluids* **24**(3), 035103 (2012). <https://doi.org/10.1063/1.3693132>
- Laizet, S., Vassilicos, J.C.: DNS of fractal-generated turbulence. *Flow Turbul. Combust.* **87**, 673 (2011). <https://doi.org/10.1007/s10494-011-9351-2>
- Laizet, S., Vassilicos, J.C.: Stirring and scalar transfer by grid-generated turbulence in the presence of a mean scalar gradient. *J. Fluid Mech.* **764**, 52–75 (2015). <https://doi.org/10.1017/jfm.2014.695>
- Laizet, S., Nedić, J., Vassilicos, J.C.: The spatial origin of  $-5/3$  spectra in grid-generated turbulence. *Phys. Fluids* **27**(6), 065115 (2015). <https://doi.org/10.1063/1.4923042>
- Lee, T.S., Ooi, E.H., Chang, W.S., Foo, J.J.: Fractal grid-induced turbulence strength characterization via piezoelectric thin-film flapping velocimetry. *Sci. Rep.* **11**, 23322 (2021). <https://doi.org/10.1038/s41598-021-02680-7>
- Li, Y., Wang, J., Zhang, P.: Effects of Gurney flaps on a NACA0012 Airfoil. *Flow Turbul. Combust.* **68**(1), 27–39 (2002). <https://doi.org/10.1023/A:1015679408150>
- Mazellier, N., Vassilicos, J.C.: Turbulence without Richardson-Kolmogorov cascade. *Phys. Fluids* **22**(7), 075101 (2010). <https://doi.org/10.1063/1.3453708>
- Measurement Specialties: LDT1-028K piezo sensor w/ leads attached. TE.com. [https://www.te.com/commence/DocumentDelivery/DDEController?Action=srchrtv&DocNm=LDT\\_with\\_Riveted\\_Leads&DocType=DS&DocLang=English](https://www.te.com/commence/DocumentDelivery/DDEController?Action=srchrtv&DocNm=LDT_with_Riveted_Leads&DocType=DS&DocLang=English) (2015). Accessed 31 Oct 2022.
- Measurement Specialties: Piezo film sensors technical manual. Sparkfun.com. <https://www.sparkfun.com/datasheets/Sensors/Flex/MSI-techman.pdf> (1999). Accessed 22 Sept 2022
- Melina, G., Bruce, P.J.K., Vassilicos, J.C.: Vortex shedding effects in grid-generated turbulence. *Phys. Rev. Fluids* **1**(4), 044402 (2016). <https://doi.org/10.1103/PhysRevFluids.1.044402>
- Mok, M.C.H., Yeoh, C.V., Tan, M.K., Foo, J.J.: Space-filling single square and square fractal grids induced turbulence: Reynolds stress model parameters-optimization. *Results Eng.* **17**, 100806 (2023). <https://doi.org/10.1016/j.rineng.2022.100806>
- Nagata, K., Sakai, Y., Inaba, T., Suzuki, H., Terashima, O., Suzuki, H.: Turbulence structure and turbulence kinetic energy transport in multiscale/fractal-generated turbulence. *Phys. Fluids* **25**(6), 065102 (2013). <https://doi.org/10.1063/1.4811402>
- Nagata, K., Saiki, T., Sakai, Y., Ito, Y., Iwano, K.: Effects of grid geometry on non-equilibrium dissipation in grid turbulence. *Phys. Fluids* **29**(1), 015102 (2017). <https://doi.org/10.1063/1.4973416>

- Nedić, J., Tavoularis, S.: Measurements of passive scalar diffusion downstream of regular and fractal grids. *J. Fluid Mech.* **800**, 358–386 (2016). <https://doi.org/10.1017/jfm.2016.385>
- Nedić, J., Supponen, O., Ganapathisubramani, B., Vassilicos, J.C.: Geometrical influence on vortex shedding in turbulent axisymmetric wakes. *Phys. Fluids* **27**(3), 035103 (2015). <https://doi.org/10.1063/1.4913573>
- Omilion, A., Turk, J., Zhang, W.: Turbulence enhancement by fractal square grids: effects of multiple fractal scales. *Fluids* **3**(2), 37 (2018). <https://doi.org/10.3390/fluids3020037>
- Rosti, M.E., Omidyeganeh, M., Pinelli, A.: Numerical simulation of a passive control of the flow around an aerofoil using a flexible, self adaptive flaplet. *Flow Turbul. Combust.* **100**(4), 1111–1143 (2018). <https://doi.org/10.1007/s10494-018-9914-6>
- Simmons, L.F.G., Salter, C.: Experimental investigation and analysis of the velocity variations in turbulent flow. *Proc. R. Soc. Lond. Ser. A* **145**(854), 212–234 (1934). <https://doi.org/10.1098/rspa.1934.0091>
- Skantham, S., Yeoh, C.V., Chin, W.M., Foo, J.J.: Forced convective heat transfer and flow characteristics of fractal grid heat sinks. *Int. J. Therm. Sci.* **125**, 176–184 (2018). <https://doi.org/10.1016/j.ijthermalsci.2017.11.016>
- Sodano, H.A., Park, G., Inman, D.J.: Estimation of electric charge output for piezoelectric energy harvesting. *Strain* **40**(2), 49–58 (2004). <https://doi.org/10.1111/j.1475-1305.2004.00120.x>
- Suzuki, H., Nagata, K., Sakai, Y., Hayase, T.: Direct numerical simulation of turbulent mixing in regular and fractal grid turbulence. *Phys. Scr.* **2010**(T142), 014065 (2010). <https://doi.org/10.1088/0031-8949/2010/T142/014065>
- Suzuki, H., Nagata, K., Sakai, Y., Hayase, T., Hasegawa, Y., Ushijima, T.: Direct numerical simulation of fractal-generated turbulence. *Fluid Dyn. Res.* **45**(6), 061409 (2013). <https://doi.org/10.1088/0169-5983/45/6/061409>
- Teh, A.L., Siow, Y.H., Chin, W.M., Chia, C.M., Foo, J.J.: Thermal mixing enhancement of a free cooling/heating system with a 2D space-filling plate. *Appl. Therm. Eng.* **89**, 946–957 (2015). <https://doi.org/10.1016/j.applthermaleng.2015.06.058>
- Tinney, C.E., Valdez, J., Murray, N.: Aerodynamic performance of augmented supersonic nozzles. *Exp. Fluids* **61**(2), 48 (2020). <https://doi.org/10.1007/s00348-019-2866-3>
- Valente, P.C., Vassilicos, J.C.: The decay of turbulence generated by a class of multiscale grids. *J. Fluid Mech.* **687**, 300–340 (2011). <https://doi.org/10.1017/jfm.2011.353>
- Weitemeyer, S., Reinke, N., Peinke, J., Hölling, M.: Multi-scale generation of turbulence with fractal grids and an active grid. *Fluid Dyn. Res.* **45**(6), 061407 (2013). <https://doi.org/10.1088/0169-5983/45/6/061407>
- Zhou, Y., Nagata, K., Sakai, Y., Suzuki, H., Ito, Y., Terashima, O., Hayase, T.: Relevance of turbulence behind the single square grid to turbulence generated by regular- and multiscale-grids. *Phys. Fluids* **26**(7), 075105 (2014). <https://doi.org/10.1063/1.4890746>